Full length article

Simulating strain localization in rolled magnesium

CrossMark

Jeffrey T. Lloyd [a], [*], Matthew W. Priddy [b]

[a] *Impact Physics Branch, U.S. Army Research Laboratory, 390 Tower Road, Aberdeen Proving Ground, MD 21005-5069, USA*
[b] *Department of Mechanical Engineering, Mississippi State University, 479-1 Hardy Road, MS 39762, USA*

ARTICLE INFO

ABSTRACT

The objective of this work was to computationally predict the interplay between material orientation, loading conditions, ductility, and failure behavior in samples hypothetically cut from a rolled plate of magnesium alloy AZ31B. Marciniak and Kuczyński analysis was used to predict failure by performing detailed finite element simulations in which imperfections are introduced at various angles to induce failure. Magnesium was represented by a reduced-order crystal plasticity model that has been shown to fit measured mechanical behavior, but is computationally efficient enough to be used in large-scale simulations and parametric studies. Plane strain tension simulations were performed on a range of material orientations, then forming limit diagrams were constructed for two selected orientations. Plane strain tension simulations indicate that for orientations where basal slip is active, the failure plane closely aligns with the basal plane. Additionally, the highest ductility was achieved by maximizing the amount of basal slip and equalizing the amount of extension twinning and non-basal slip. In magnesium, failure behavior is shown to strongly correlate with material orientation and the relative activity of deformation mechanisms. Comparison of the two forming limit diagrams highlighted the deficiency of using a single measure for ductility: although these orientations possessed similar strain to failure under plane strain tension this did not correlate with ductility under more complex loading conditions.

Published by Elsevier Ltd on behalf of Acta Materialia Inc.

1. Introduction

Magnesium alloys have the potential to replace other lightweight metals due to their high strength and low density (1.74 g/cm^3). However, many magnesium alloys have shown a propensity for strain localization and failure, and exhibit relatively low ductility compared to other lightweight structural metals with comparable specific strength, e.g., high-strength aluminum alloys. Macroscopically, magnesium exhibits pronounced plastic anisotropy, wherein the material's initial yield strength and subsequent strain hardening rate strongly depends on how the loading direction relates to the material's processing directions, which is thought to limit its ductility. The plastic anisotropy is due to the inelastic behavior of prevalent deformation mechanisms, which themselves possess disparate initial strengths and subsequent hardening rates. Altering microstructural features such as grain size, alloy content, and precipitate distribution through thermomechanical processing has been shown to influence ductility in a secondary role; however,

modifying bulk texture and its relation to principle loading directions is the dominant characteristic that governs ductility in magnesium alloys [1–9].

Processing methods used to improve tensile elongation to failure by modifying bulk texture in magnesium can generally be classified into two methods: (i) those that decrease peak texture intensity and (ii) those that reorient the macroscopic texture. By adding rare earth elements to magnesium, the c/a ratio is reduced and can approach that of an ideal hexagonal close-packed (HCP) crystal, e.g., $c/a = 1.624$ [10]. The increased crystal symmetry has been shown to reduce peak texture intensity during processing, which produces a material that exhibits reduced plastic anisotropy and increased tensile elongation to failure [5,11,12]. However, this increased tensile elongation to failure does not necessarily translate to increased ductility under other loading conditions, such as during deep drawing [13]. Peak texture intensity reduction has also been shown to occur during non-equilibrium process methods such as rapid solidification. In the spinning water atomization process (SWAP), fine powders were created via SWAP and subsequently extruded to produce magnesium alloys with fine grains (1–2 μm), low peak texture intensity, and moderate tensile elongation prior to failure [7]. Unlike the previous two methods, equal

channel angular extrusion (ECAE) produces peak textures that result in an equal or greater intensity than conventional forming processes, which are reoriented with respect to the original material's texture. Several ECAE routes have been shown to produce materials with superior strength and similar or improved elongation to failure over conventionally rolled or extruded alloys [1,8,9]. Similar macroscopic texture reorientation can be achieved during friction stir processing, which creates a strongly reoriented texture in the process zone that gradually decreases in regions away from the affected region. For processing methods that reorient the texture but do not reduce peak intensity, gains in elongation to failure are achieved because the peak texture and sample directions no longer coincide. However, if samples are cut from the as-processed material so that they are loaded along their principal texture components instead of material processing directions, large reductions in tensile elongation prior to failure have been observed [8]. Because a measure of ductility is strongly dependent on the interplay of texture and loading directions, it is desirable to develop an analytical or computational framework that can be used to find the optimal texture that maximizes ductility for a given set of loading conditions.

Defining a specific value for the ductility is difficult either from experimental viewpoint or as a mathematically derived quantity. Ductility is often referred to for a specific problem of interest, and may include quantities such as deep drawing ratio, minimum bend radius, or elongation prior to failure. The most commonly used quantity is tensile elongation prior to failure. In quasistatic, uniaxial tension tests, a variety of easy-to-interpret macroscopic ductility measures are commonly used. For ductile materials, the critical strain for Considère's criterion, $\varepsilon_c = d\sigma/d\varepsilon = \sigma$, is less than the strain corresponding to the ultimate tensile stress $\varepsilon_{max} = d\sigma/d\varepsilon = 0$, which is less than the total strain to failure, ε_f; yet, all three of these are reasonable measures of ductility for this simple loading case. Physically, localization in the specimen can occur due to geometric thinning or necking, material softening, imperfection-induced localization, or a combination thereof, and does not necessarily correspond to any of the aforementioned strain measures. For more complex loading cases, such as multiaxial deformation or dynamic loading, effects such as hydrostatic pressure and inertial effects also influence ductility.

Most analytical or computational theories identify the onset of localization following arguments of bifurcation or non-uniqueness; however, they differ in how the instability itself is initiated. Bifurcation theory originates from the concept that "stationary discontinuities" act as localization sites in the material. Alternatively stated, localization occurs in a band of material if the traction rate acting on the band is stationary with respect to extension and shear within the band [14]. Hill analyzed localization in elastic-plastic solids [15] then Rice [14] extended this work to analyze pressure-sensitive materials, cross-slip in single crystals, and vertex yield effects. Although this method is useful and has received significant attention in literature, failure in ductile materials has also been shown to occur both prior to, and after such conditions have been met [16]. Marciniak and Kuczyński (MK) analysis differs in that it assumes failure occurs by concentrations of strains initiated at imperfections[1] and identifies the failure strain as the value where the strain rate in the imperfection and bulk material diverge [16–18]. MK analysis was initially used to identify the failure strains for biaxial loading in sheet metal by specifying a thinned region

with fixed angle relative to the loading directions. Hutchinson and Neale [19] extended this analysis to include that the imperfection may lie on an arbitrary angle with respect to the loading axis, and analyzed this for plane strain as well as general loading cases. This method has also been used to analyze single crystals as well as polycrystalline ensembles [20].

In this work, we analyze the correlation between material orientation and failure in rolled magnesium samples by performing full finite element simulations of MK specimens. Initially, we analyze a broad range of textures undergoing plane strain, uniaxial tension at moderate loading rates to determine how texture dictates failure under a single loading condition. By using a reduced-order polycrystalline magnesium model, we are able to analyze all possible orientations with relatively little computational cost, yet retain microstructural information to relate failure strains to activity of different deformation mechanisms. Then, we create forming limit diagrams (FLDs) for two polycrystalline textures that possess similar predicted failure strains to understand how ductility determined from uniaxial data relates to ductility under more complex loading conditions.

2. Methods

2.1. MK analysis

This analysis closely mirrors that by Hutchinson and Neale [19] in that we introduce a groove of material with angle θ that is inclined with respect to the loading direction. The groove has a reduced thickness compared to the surrounding region. Unlike previous work, a full finite element description is retained within the groove as well as the surrounding region. The mean strain rate within the groove is compared with the bulk to determine the limiting strain, e.g., the onset of strain localization. Strain localization is defined to occur when volume-averaged plastic strain rate inside the grooved region is 10 times that in the bulk, a ratio that has been used in previous studies [21]. Varying this ratio alters the total strain to failure in a straightforward manner, but does not influence qualitative trends. The plastic strain rate is calculated for a volume within the grooved region and for volumes above and below the grooved region, where care was taken to define the volumes to avoid elements close to surfaces.

Abaqus/Explicit 6.10 was used for all of the simulations in this study [22]. The consistent units used for Abaqus in these simulations are given in Table 1. The geometry of the rectangular bar specimens with a groove are shown schematically in Fig. 1. The groove is used to represent a hypothetical defect that exists in the material and could initiate a local instability. Tensile loading is applied in the y-direction. The specimens contained between 20,000 (0°) and 30,420 (60°) hexahedral elements (type C3D8RT) depending on the groove angle. The overall dimensions of the specimens are 10.0 mm tall, 2.0 mm wide, and 1.0 mm thick, with a 1.0 mm groove height for all simulations. The applied strain rate in all cases is 100.0 s^{-1} and all simulations are run to a maximum

---

[1] Imperfections may be descriptions of real physical imperfections or as surrogates used to mimic the effect of imperfections throughout the material. Although imperfection size and magnitude may affect quantitative measurements of ductility, it often does not affect qualitative trends.
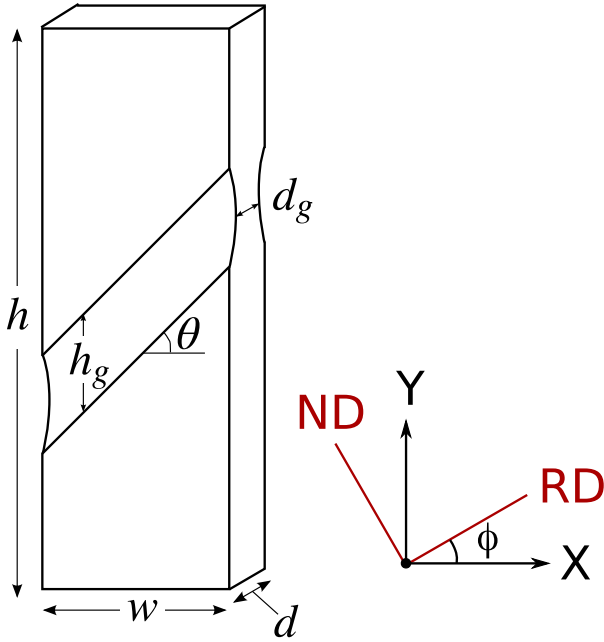
Table 1
Consistent units used in Abaqus for this study.

Quantity	Units
Length	μm
Force	μN
Mass	ng
Time	μs
Stress	MPa
Energy	pJ
Density	ng/μm^3

Fig. 1. Schematic for plane strain and biaxial loading specimen. Specimen contains pre-notched groove section with angle θ. The angle ϕ is used to vary the material orientation from its natural plate directions. Sample dimensions are quantified in Table 2.

applied strain of 40.0%. Additional simulation specifications are summarized in Table 2. Each element of the three-dimensional specimen is assigned a unique orientation. This gives a mesh where each element represents a single grain in a polycrystal. These orientations are randomly sampled from X-Ray diffraction patterns measured on rolled AZ31B using the software MTEX [23]. The measured pole figure and 300 representative orientations are shown in Fig. 2. A two-step approach is used in this work: identify the influence of material orientation on the plane strain tensile failure behavior; and generate FLDs for particular material orientations to determine how ductility measured from a single loading condition relates to ductility in more complex loading cases.

Plane strain tension is modeled by prescribing a constant velocity to the $\pm y$ faces while the $\pm x$ faces are held fixed in the x direction. No other boundary conditions are applied, i.e., the z-faces are considered free surfaces in this study. In these simulations we iterated over (i) material direction and (ii) potential groove angles. The material direction ϕ was varied in 5° increments such that the plate normal direction (ND) ranged from 0°, in which the ND coincided with the tensile axis, to −90°, in which the ND coincided with the horizontal direction, as seen in Fig. 1. In addition to varying the material's orientation, the groove angle θ was varied over $\pm 60°$

Table 2
Geometric details for grooved specimen simulations.

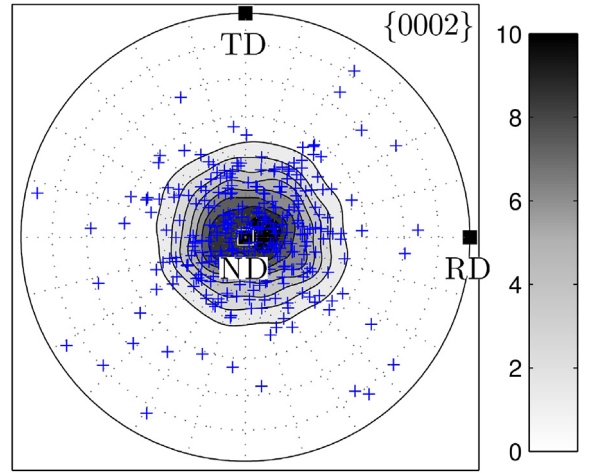| Variable	Value
Maximum applied strain	0.4 $\mu m/\mu m$
Macroscopic strain rate	100.0 s^{-1}
Simulation time	2000.0 μs
Specimen height (h)	10.0 mm
Specimen width (w)	2.00 mm
Specimen depth (d)	1.00 mm
Groove height (h_g)	1.00 mm
Groove depth (d_g)	0.80 mm
Groove angle (θ)	−60° to 60°

Fig. 2. Basal pole figure for rolled AZ31B showing measured X-Ray diffraction intensities via grayscale contours and 300 randomly sampled discrete orientations.

in 5° increments to ensure all potential failure angles were accounted for in the analysis. In all, a total of 925 simulations plane strain tension simulations were performed.

To generate FLDs, a velocity was applied to $\pm y$ and $\pm x$ faces such that the ratio of the velocities (v_x/v_y) ranged from −0.5 to 1.0, with 31 velocity ratios used to discretize the range of loading conditions. These velocities increased with increasing deformation to maintain a constant macroscopic strain rate in both directions. For the FLDs, θ was varied over $\pm 60°$ in 15° increments. In total, 279 simulations were performed to generate each FLD.

2.2. Reduced-order model

An orientation-dependent material description is essential for capturing the anisotropic mechanical response of strongly textured magnesium alloys. The primary deviation of crystal models for hcp metals from more conventional crystal fcc models [24] is the method that is used to treat twinning. The inelastic component of the velocity gradient is decomposed into shear on the twinned and untwinned lattices, e.g., $\mathbf{L}^P = \mathbf{L}^P_{\text{untwinned}} + \mathbf{L}^P_{\text{twinned}}$. Twinning is often treated as a form of "pseudo-slip" wherein twin variants are either prohibited [25] or allowed [26,27] to reorient the lattice. For the case where twinning reorients the lattice these components are

$$\mathbf{L}^P_{\text{untwinned}} = \left(1 - \sum_{\beta=1}^{N_{\text{twin}}} f^\beta_{\text{twin}} \right) \sum_{\alpha=1}^{N_{\text{slip}}} \dot{\gamma}^\alpha_{\text{slip}} \left(\mathbf{s}^{(\alpha)}_{\text{slip}} \otimes \mathbf{m}^{(\alpha)}_{\text{slip}} \right)$$
$$+ \sum_{\beta=1}^{N_{\text{twin}}} \dot{\gamma}^\beta_{\text{twin}} \left(\mathbf{s}^\beta_{\text{twin}} \otimes \mathbf{m}^\beta_{\text{twin}} \right) \tag{1}$$

and

$$\mathbf{L}^P_{\text{twinned}} = \sum_{\beta=1}^{N_{\text{twin}}} f^\beta_{\text{twin}} \sum_{\alpha=1}^{N_{\text{slip}}} \dot{\gamma}^\alpha_{\text{slip}} \left(\mathbf{s}^{*(\alpha)}_{\text{slip}} \otimes \mathbf{m}^{*(\alpha)}_{\text{slip}} \right), \tag{2}$$

where f^β denotes the volume fraction of material twinned due to twin system β, whereas $\dot{\gamma}^\alpha$, $\mathbf{s}^\alpha$ and $\mathbf{m}^\alpha$ denote the shearing rate, slip (or pseudo-slip) direction, and normal of deformation mechanism α. In the case where reorientation is not modeled, such as in Ref. [25], the velocity gradient simplifies to

$$\mathbf{L}^P = \sum_{\alpha=1}^{N_{\text{slip}}} \dot{\gamma}_{\text{slip}}^{\alpha} \left(\mathbf{s}_{\text{slip}}^{(\alpha)} \otimes \mathbf{m}_{\text{slip}}^{(\alpha)} \right) + \sum_{\beta=1}^{N_{\text{twin}}} \dot{\gamma}_{\text{twin}}^{\beta} \left(\mathbf{s}_{\text{twin}}^{\beta} \otimes \mathbf{m}_{\text{twin}}^{\beta} \right). \qquad (3)$$

Iteratively solving for the amount of slip and twinning is computationally costly, but can be done in a reasonable manner [28]. In addition to computational cost, accurately modeling the competition between twin-driven domain refinement and dislocation-based slip, and how these mechanisms are influenced by processing history and loading conditions is difficult; however, some physics-based constitutive relations have shown significant promise [29—31]. Although complex models for magnesium have been used to study localization and failure, to date, they have only been implemented into a homogenized framework, e.g., Taylor of self-consistent formulations [32—34]. In a homogenization scheme, stresses are computed for each grains but they are assumed to undergo a uniform deformation field that is based on a weighted average of the individual mechanical response of the poly-crystalline ensemble. Spatially heterogeneous deformations arising from grain-grain interactions are neglected in such a framework. These authors point out that direct numerical simulating a poly-crystalline aggregate in a finite element framework with such models is computationally burdensome. The problem is rendered tractable by approximating the MK analysis using a homogeniza-tion scheme [35]. In contrast to using a computationally costly model with a simplified geometric description, we retain a full geometric description of the MK analysis geometry and use a computationally efficient crystal model, which is derived by mak-ing a number of simplifications to existing crystal models.

The reduced-order crystal model has been elaborated upon elsewhere, so only pertinent features are discussed [36]. Extension twinning is treated as pseudo-slip, but reorientation effects are not included. The combination of prismatic and pyramidal slip systems is captured using a single, von Mises yield surface [37]. The aggregate behavior of the 3 basal slip systems is combined into a single system that acts in the direction of maximum resolved shear stress on the basal plane. Extension twinning and basal slip are assumed to be rate-independent mechanisms, whereas nonbasal slip is assumed to be rate-dependent. As a result, the reduced-order model has an inelastic velocity gradient that can be viewed as a simplified version of Eq. (3), e.g.,

$$\mathbf{L}^P = \frac{3 \dot{\bar{\varepsilon}}_{\text{nbslip}}}{2 \sigma_{\text{vm}}} \boldsymbol{\sigma}' + \dot{\gamma}_{\text{basal}} (\mathbf{s}_{\text{basal}} \otimes \mathbf{m}_{\text{basal}})$$
$$+ \sum_{\beta=1}^{N_{\text{twin}}} \dot{\gamma}_{\text{twin}}^{\beta} \left(\mathbf{s}_{\text{twin}}^{\beta} \otimes \mathbf{m}_{\text{twin}}^{\beta} \right), \qquad (4)$$

where σ_{vm} and $\dot{\bar{\varepsilon}}_{\text{slip}}$ denote the isotropic, Von Mises effective stress and plastic strain rate, respectively. Note summation only occurs over twin systems, as other slip mechanisms have been combined into aggregate deformation mechanisms.

Because of these assumptions, computational time for the model is only approximately five times slower than an isotropic, rate-dependent strength model, and ranges from several times to orders of magnitude faster than existing hcp crystal models, depending on the kinematic assumptions employed. This model has been shown to be able to reproduce mechanical behavior of pure Mg single crystals, rolled AZ31B plates, as well as extruded AMX602 plates reasonably well [36,38]. In this work, model pa-rameters for rolled AZ31B are the same as those used in Ref. [36].

3. Results

3.1. Uniaxial plane strain simulations

In Fig. 3 all combinations of groove angle θ and orientations ϕ are plotted according to their strain to failure. Because the di-mensions of the groove dictate the particular value of the failure strain, only relative trends between groove angle and material orientation are discussed. For each value of ϕ, the minimum of the plotted values corresponds to the predicted failure strain for that orientation. Of all the orientations there are two global extrema as well as two local extrema: the global minimum failure strain is at $-90°$, which corresponds to tension along the RD; the global maximum failure strain is at $-70°$; there is a local minimum between $-30°$ to $-35°$; and there is a local maximum at $0°$, which corresponds to tension along the ND.

For each orientation, there are several groove angles that give nearly an identical failure strains. Because discretized polycrystal FEM simulations are intrinsically stochastic, i.e., grain-grain in-teractions and their clustering inside or outside the grooved region may differ for various instantiations, it is expected that some variability may occur between simulations. Therefore, in Fig. 4, groove angles that fall within 5% of the relative minimum strain to failure for each orientation are plotted. Additionally, a schematic illustrating the interplay between mean groove angle that causes failure and the corresponding idealized single crystal orientation representing the rolled polycrystal are plotted in Fig. 5 for select orientations.

For orientations with $-60° \leq \phi \leq 0°$, the groove angles that promote localization fall within a band that spans approximately $40°$. This implies a range of hypothetical imperfections orientations will give similar localization behavior. For angles $-90° \leq \phi \leq -60°$ the spread tightens but still gives a range of orientations that cause failure. Based on the schematic shown in Fig. 5, for orientations where there is some resolved shear stress on the basal plane, the minimum groove angle to promote localization lies close to the basal plane orientation, albeit with some deviation. If there were a direct 1:1 correlation between ϕ and θ from $-60°$ to $0°$, it would imply that the groove angle that causes failure rotates to maximize the contribution of basal slip in the groove; however, the difference in angles implies this is not the case. Basal slip alone cannot provide
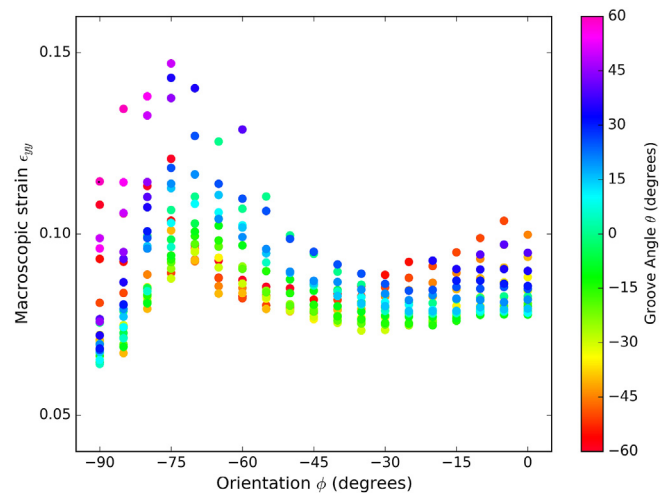

Fig. 3. Macroscopic strain in which the strain rate in the groove divided by the strain rate in the bulk begins to diverge, for simulations with varying orientation and groove angle. We define that divergence occurs when the ratio of these values exceeds 10:1, as indicated in the text.
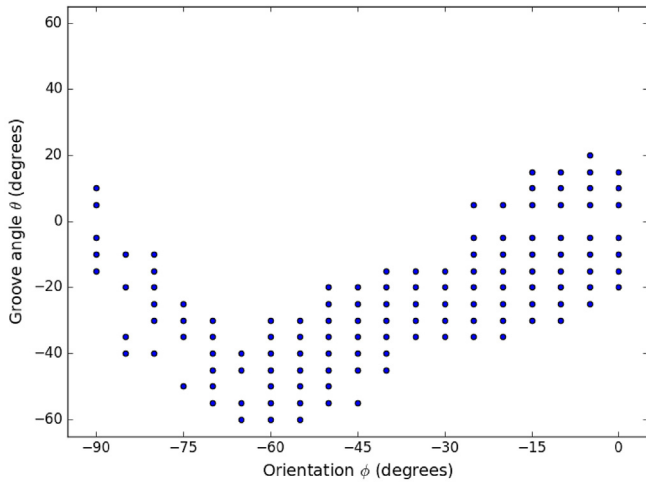
Fig. 4. Groove angles that give a macroscopic failure strain within 5% of the minimum failure strain for each orientation.
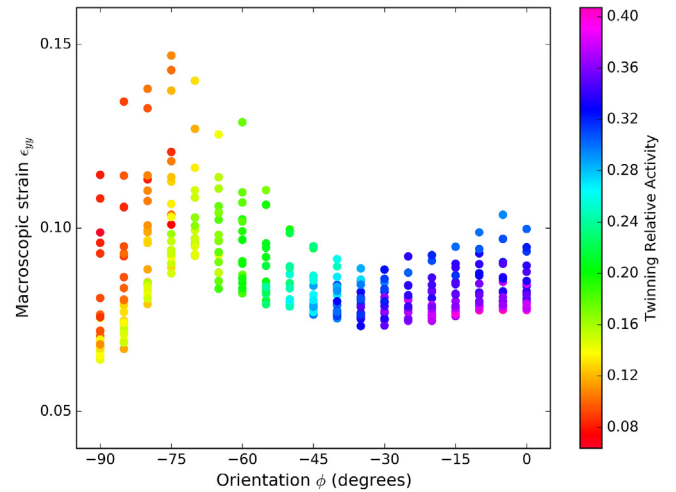

Fig. 6. Relative activity of twinning plotted as a function of orientation and macroscopic failure strain. Relative activity of deformation mechanisms is defined in Eq. (5).

compatibility between the groove and the bulk. Instead, the contribution of extension twinning and basal slip are maximized in this band, and the groove angle rotates accordingly. This will be discussed in more detail in Section 4. Note that for the case of $\phi = 0°$ and $\phi = -90°$, there is no resolved shear stress on the basal plane for the idealized case, and thus the corresponding average groove angle is approximately $0°$. These trends imply that for plane strain tension the material will be most sensitive to localization when an imperfection lies along the basal plane. The opposite holds true as well: materials will be least sensitive to imperfections that lie perpendicular to the basal plane. Although the preceding analysis gives the geometric relation between groove angle and material orientation, it does not clarify why different orientations possess differing failure strains. To understand the magnitude of failure strains, it is helpful to quantify the relative contribution of each deformation mechanism to the total deformation.

The relative activity at each integration point is the ratio of total shear activity of the slip/twin system to the sum of total shear on all slip and twin systems at a given time increment, i.e.,

$$\bar{r}^{(\alpha)} = \frac{r^{(\alpha)}}{\sum_\beta r^{(\beta)}}, \qquad (5)$$

where $r^{(\alpha)}$ is the volume-averaged, accumulated inelastic shear strain due to the αth deformation mechanism at each integration point [25,39]. In this case volume averaging is performed within the grooved region. The relative activity of extension twinning, basal slip, and non-basal slip are plotted in Figs. 6–8.

Fig. 6 shows that for $\phi = 0°$, nearly all groove angles possess twinning as a dominant deformation mode. Increased twinning activity gives a local maximum in the strain to failure occurs for $\phi = 0°$, but the failure strain does not differ significantly for orientations $-45° \leq \phi \leq 0°$. Fig. 7 indicates that basal slip is active for all loading cases. Orientations where basal slip has the highest relative activity, e.g., cases with $-70° \leq \phi \leq -45°$, which correspond to the highest macroscopic strain to failure; however, this appears to be of secondary importance. Of the cases where basal slip is most active, the orientations where the relative activity of
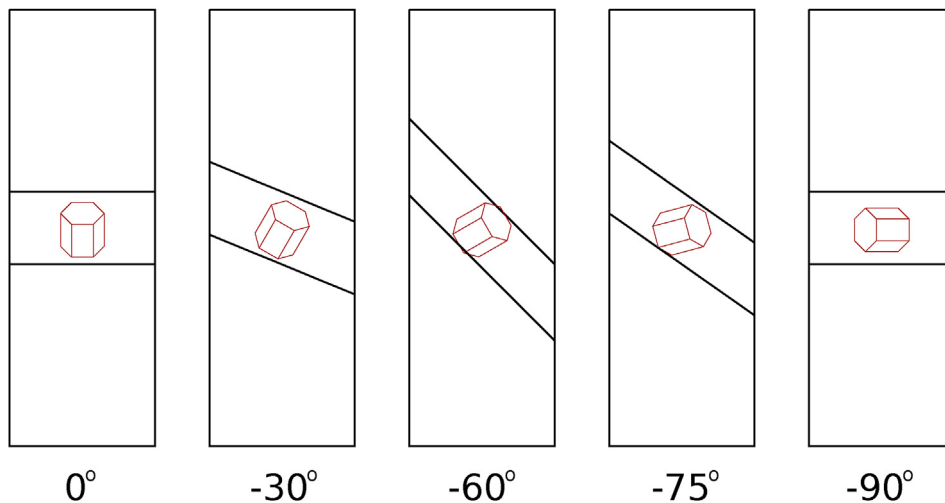

Fig. 5. Schematic illustrating selected angles for ϕ and the corresponding mean groove angle θ that causes failure. The hcp unit cell is used to represent the ideal rolling texture, wherein the $\vec{c}$ axis is aligned with the ND.
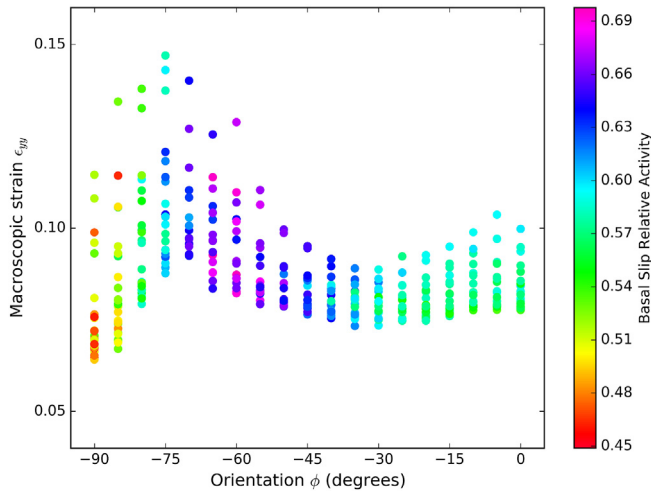
Fig. 7. Relative activity of basal slip plotted as a function of orientation and macroscopic failure strain. Relative activity of deformation mechanisms is defined in Eq. (5).
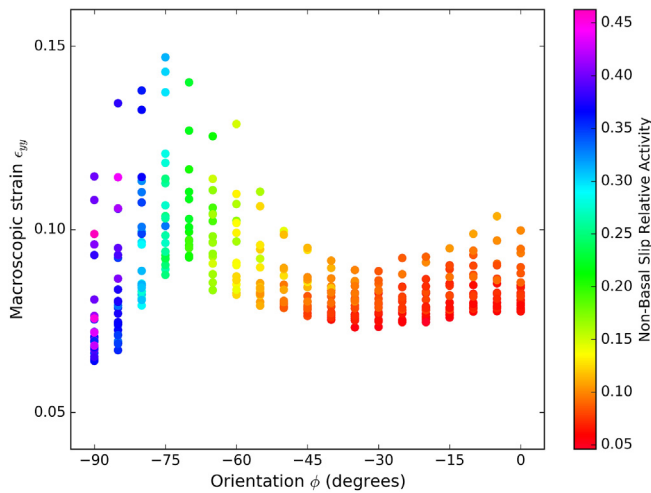

Fig. 8. Relative activity of non-basal slip plotted as a function of orientation and macroscopic failure strain. Relative activity of deformation mechanisms is defined in Eq. (5).

extension twinning and non-basal slip are equivalent give the highest ductility. In contrast, Fig. 8 shows that of all the orientations, the one that has the highest relative activity of non-basal slip has the lowest ductility, e.g., when the tension is applied along the RD.

3.2. Forming limit diagrams for select orientations

As discussed in Section 2.1, FLDs were constructed for two orientations with similar failure strains but different orientations. For this we chose $\phi = 0°$ and $\phi = 45°$ because they possess different dominant deformation mechanisms. Note that these orientations are not "sheet" directions: most experimental FLDs are generated in the RD-TD plane. The point of this analysis is to highlight effects of an isotropy, so variations in the RD-ND plane are chosen to maximize anisotropy. For several loading conditions, both samples did not reach the 10:1 localization criterion, so only results wherein localization occurred are plotted. Of all the simulations that did localize, the locust of points falling along the minimum values of ϵ_{yy} for given values of ϵ_{xx} are those that constitute the FLD.
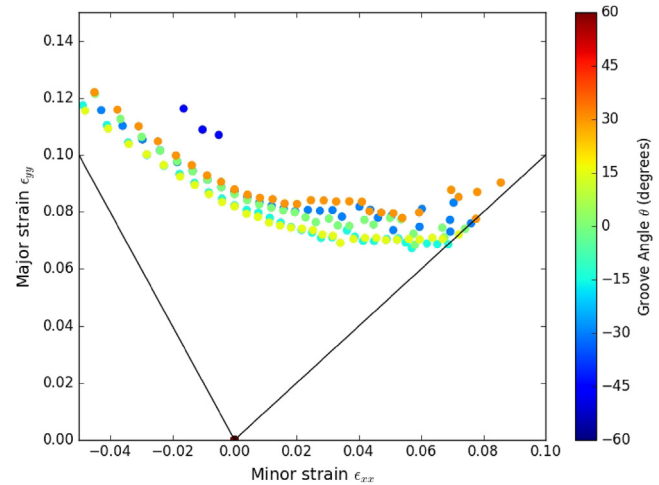

Fig. 9. FLD for $\phi = 0°$. Lines are used to indicate uniaxial and equi-biaxial extension.

Fig. 9 depicts the FLD for the case where tension along the major axis is coincident with the ND and loading along the minor axis is coincident with the RD ($\phi = 0°$). For all of the loading conditions, the material is observed to possess similar localization strains for $-30° \leq \theta \leq 30°$. Experimental FLDs for isotropic materials often possess a minimum value of ϵ_{yy} at $\epsilon_{xx} = 0$, with much higher failure strains for $\epsilon_{xx} < 0$ and slightly higher failure strains for $\epsilon_{xx} > 0$ [40]. In contrast, more anisotropic materials such as Ti–-6V–-4Al may possess a similar FLD [41] shape to that seen in Fig. 9, where there is increased ductility for $\epsilon_{xx} < 0$ as loading approaches uniaxial tension, but little discernible change in ductility for $\epsilon_{xx} > 0$ as loading approaches biaxial tension.

In contrast, consider the FLD shown in Fig. 10 for $\phi = -45°$. Unlike the previous case, this orientation only localizes for negative groove angles. Groove angles of $-45° \leq \theta \leq -30°$ minimize the failure strain for all loading cases. Unlike conventional isotropic materials, the simulations predict that the strain to failure decreases as ϵ_{xx} becomes more positive. Even though $\phi = -45°$ has a similar failure strain as $\phi = 0°$ in plane strain tension, it possesses a slightly higher failure strain for cases where $\epsilon_{xx} < 0$, but a much lower failure strain for $\epsilon_{xx} > 0$. The trend of decreasing failure strain as ϵ_{xx} becomes more positive is *not* observed in most metals, and is
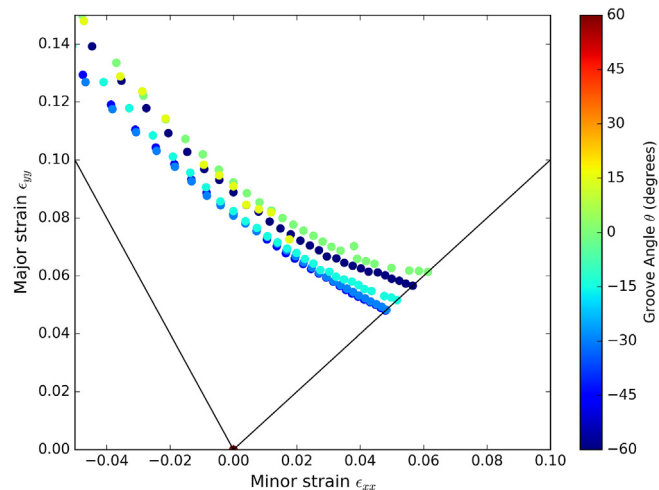

Fig. 10. FLD for $\phi = -45°$. Lines are used to indicate uniaxial and equi-biaxial extension.

elaborated upon in the following section in terms of existing analytical and experimental trends.

4. Discussion

There is a well-founded theoretical basis for predicting strain localization and forming limits in FCC and BCC metals that exhibit relative inelastic isotropy [40]; however, anisotropy of the initial yield strength and subsequent strain hardening behavior in rolled Mg polycrystals complicates their analysis. Several predictions in this work differ from those observed for isotropic materials: failure angles in plane strain tension are strongly coupled to material orientation; failure strains in plane strain tension correlate with activity of particular deformation mechanisms; and FLDs may possess either constant or even decreasing strain to failure along the major axis as the minor axis strain is increased beyond 0 towards biaxial extension.

In this work we examined how material orientation, which governs apparent plastic anisotropy, gave failure along varying groove angles. For cases of $\phi = 0°$ and $\phi = -90°$ the minimum groove angle is approximately $0°$, with no preference in the direction of inclination. For these cases, either profuse extension twinning or non-basal slip occur, respectively, and the material can accommodate the majority of deformation with these mechanisms with relatively little plastic anisotropy. For isotropic as well as anisotropic materials, macroscale plasticity theories generally predict that for plane strain tension, the minimum groove angle is $0°$ [40,42]. Kuroda and Tveergard showed that for FCC polycrystals the groove angle weakly depends on the material's preferred orientation [43]. However, Figs. 4 and 5 indicate that for plane strain tension, the failure angle closely follows the basal plane as the material's orientation is decreased from $\phi = 0°$. As ϕ becomes more negative so does θ: no positive values of θ give failure for $-85° \leq \phi \leq -30°$.

To understand why failure occurs primarily for negative values of θ, the case of $\phi = -60$ is examined with two groove angles of $\theta = \pm45°$. The relative volume fraction of twinning and accumulated plastic strain due to basal slip for these cases are plotted in Fig. 11. Fig. 11 indicates for $\theta = -45°$, which causes failure, twinning occurs profusely within the groove whereas basal slip occurs at an angle of $-60°$, which is slightly inclined with respect to the groove. Together, these two mechanisms provide sufficient deformation for the groove to deform independently from the bulk material, which causes localization. Note basal slip alone would not be able to provide sufficient deformation to localize the groove region since it provides negligible displacement in the groove normal direction. For $\theta = 45°$ twinning occurs homogeneously in and outside of the groove. Some basal slip occurs in bands spanning in and normal to the groove to provide some normal displacement within the groove. However, inhomogeneous deformation bands are distributed throughout the bulk of the sample and suppress localization by providing additional compatibility to the bulk deformation. Note that it is improbable that a homogenized method would be able to capture such behavior. From these simulations, for $\phi = -60°$ and other orientations where basal slip is active, the minimum groove angle that causes failure is the angle that maximizes the combination of extension twinning and basal slip in the groove.

In this work we correlated failure and orientation from a purely mechanistic standpoint, and related this to the relative activity of mechanisms. We predicted that ductility was highest in plane strain tension for orientations wherein the amount of basal slip was maximized and both extension twinning and non-basal slip were proportional. This result is consistent with results from Agnew and colleagues [1], who showed that as the inclination of the basal pole increased from conventionally extruded orientations (where the tensile and basal poles are perpendicular, resulting in profuse pyramidal slip) ductility increased. The authors also showed that texture is of primary importance in dictating the eventual failure, with effects such as grain size playing only a secondary role. We showed that plane strain tension simulations where non-basal slip
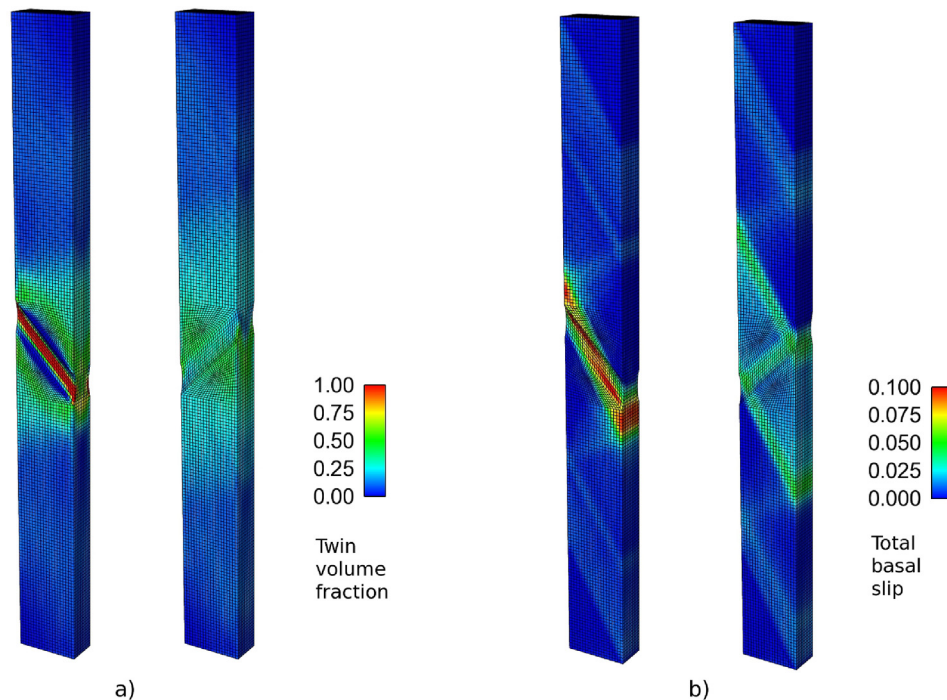

Fig. 11. Accumulated (a) volume fraction of twinning and (b) basal slip in plane strain tension simulations with groove angles of $\theta = \pm45°$. Note that specimens localize at lower strain levels for $\theta = -45°$, which are plotted on the left for both images.
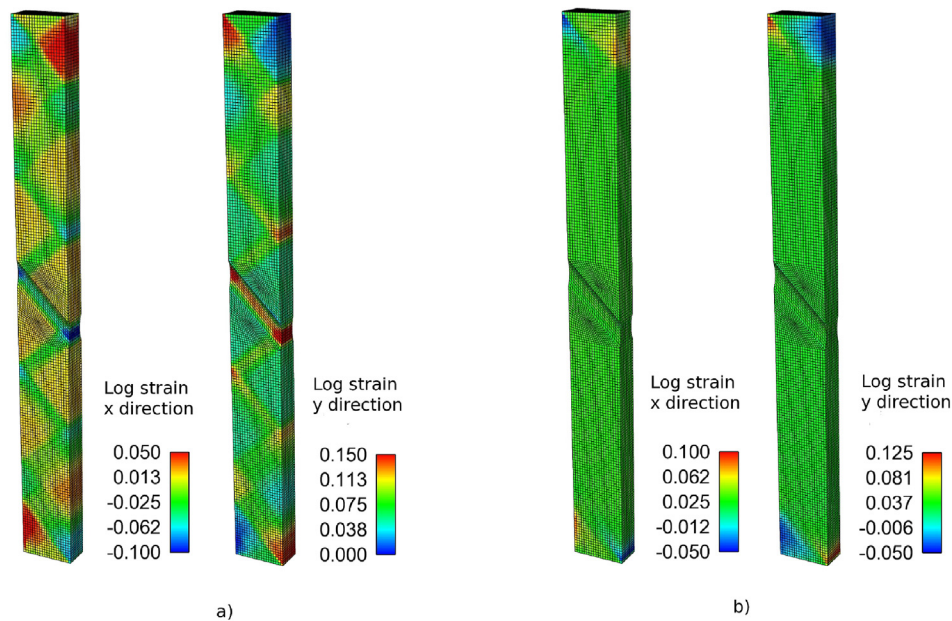
Fig. 12. Logarithmic strain plotted for both major and minor directions in the case of $\phi = -45°$ and $\theta = -45°$ loaded in (a) plane strain tension and (b) equi-biaxial tension. Both plots are taken immediately prior to failure, which occurs at different macroscopic strains.

dominated had the lowest ductility. Plane strain compression of single crystal Mg showed deformation conditions in which pyramidal slip dominated had much lower ductility than those where extension twinning dominated deformation [44]. Additionally, uniaxial compression experiments of fine-grained magnesium AZ31B showed a similar trend that deformation due to pyramidal slip alone limited ductility substantially [8].

Despite these cases that agree with simulations, there are physics lacking from the purely mechanistic analysis. Al-Samman and Gottstein observed loading conditions that promoted profuse extension twinning gave the lowest ductility for plane strain compression of extruded Mg at room temperatures [6]. Additionally, molecular dynamics simulations by Wu and Curtin suggest that increasing availability and mobility of dislocations that can accommodate $\vec{c}$ axis deformation via cross-glide, which is greatly influenced by alloying, has the potential to greatly enhance ductility in hcp metals [45,46]. Neither interface creation nor cross-glide are treated in a sophisticated manner in the current framework. Including effects is anticipated to be costly from a computational standpoint, but should give more accurate predictions of localization propensity in magnesium alloys.

In contrast to our method, homogenization methods employing crystal plasticity models have been used to study forming limits of Mg alloys subjected to biaxial loading in the RD-TD plane [32–34,47]. These simulations predict either increasing or constant major strain to failure for increasing positive values of minor strain. Analytical predictions for most isotropic materials, which are well-described using Hosford's yield criterion with exponent $m < 17.7$, give increasing strain to failure for increasing positive values of minor strain [40,48]. Numerous experimental FLDs have been determined for AZ31B in the RD-TD plane and give similar relations to computational models at room and elevated temperatures [49–52]. In this work we chose to examine the RD-ND plane due to its plastic anisotropy: variations in orientation should give more pronounced differences in FLD predictions. The case with $\phi = 0°$ shows little dependence of the failure strain with increasing minor strain, which appears to be consistent with the aforementioned experimental and computational studies; however, for $\phi = -45°$,

additional transverse tension caused a decrease in the maximum forming limit strain. To the authors' knowledge, the only Mg alloy that has been shown to exhibit such behavior is ZEK-100-O, which was reported to follow a similar trend [53]. The addition of 0.2% wt Nd gives the material a more diffuse texture than AZ31B, where the peak basal pole is inclined approximately 40° from the ND to the TD, and 20° from the ND to the RD [54]. An alternative study on ZE10 (0.2% Ce, 0.1% La by wt) did not have this same trend, however, despite its similar texture [34].

To understand why the material is able to localize more readily in plane strain tension than equi-biaxial tension for $\phi = -45°$, the logarithmic strain of the major and minor stress components are plotted for both cases with $\theta = -45°$ in Fig. 12. For plane strain tension, although deformation is concentrated within the groove, it is also accommodated in the bulk via intense deformation bands separating regions that remain relatively free of deformation. The spatially inhomogeneous deformation allows the material to accommodate strains normal to the groove without increasing the stress in the groove significantly. For equi-biaxial tension the specimens deform homogeneously within and outside of the groove region. This homogeneous deformation causes more rapid failure, as would be the case for a material that exhibits isotropic deformation. Additional experimental studies are needed to determine if the FLD predictions for $\phi = -45°$ are indeed physical, or if other failure mechanisms not modeled by the MK analysis activate in the material for this particular loading condition. Note from examining Fig. 12, it is not surprising that the present analysis deviates from predictions from homogenized methods, as the bulk material contains spatially inhomogeneous deformation patterns to provide aggregate compatibility, and which would be smeared out using an averaging method.

5. Conclusions

Plane strain simulations were used to explore the role that the relative orientation of the basal pole to the loading axis played in the failure process of rolled AZ31B. FLDs were constructed for two orientations that had similar failure strains to understand if they

their ductility would be comparable for a range of biaxial loading conditions. Based on these simulations, the following observations were made for rolled AZ31B:

- Use of hybrid crystal-macroscale plasticity models allows full finite element discretization of MK analysis without employing homogenization techniques, which may smooth out inhomogeneous deformation patterns observed in both the groove and the bulk in MK analysis.
- Failure strains were highest when the amount of twinning and non-basal slip were nearly identical, and basal slip provided the majority of deformation.
- Failure strains were lowest when non-basal slip was the primary deformation mechanism.
- In plane strain tension, for orientations where basal slip was active, failure angles closely aligned with the basal plane and did not occur along the basal normal.
- Although orientations $\phi = 0°$ and $\phi = -45°$ had similar ductility under uniaxial plane strain conditions, they had significantly different ductilities under various biaxial loading conditions.
- Failure behavior of the $\phi = -45°$ orientation displayed decreasing ductility as the minor strain increased from 0 to equi-biaxial tension, in stark contrast to experimentally-determined FLDs observed for most metals.

Acknowledgment

References

[1] S.R. Agnew, J.A. Horton, T.M. Lillo, D.W. Brown, Enhanced ductility in strongly textured magnesium produced by equal channel angular processing, Scr. Mater. 50 (3) (2004) 377—381.

[2] R. Gehrmann, M.M. Frommert, G. Gottstein, Texture effects on plastic deformation of magnesium, Mater. Sci. Eng. A 395 (1) (2005) 338—349.

[3] P. Mehrotra, T.M. Lillo, S.R. Agnew, Ductility enhancement of a heat-treatable magnesium alloy, Scr. Mater. 55 (10) (2006) 855—858.

[4] W. Woo, H. Choo, D.W. Brown, P.K. Liaw, Z. Feng, Texture variation and its influence on the tensile behavior of a friction-stir processed magnesium alloy, Scr. Mater. 54 (11) (2006) 1859—1864.

[5] J. Bohlen, M.R. Nürnberg, J.W. Senn, D. Letzig, S.R. Agnew, The texture and anisotropy of magnesium—zinc—rare earth alloy sheets, Acta Mater. 55 (6) (2007) 2101—2112.

[6] T. Al-Samman, G. Gottstein, Room temperature formability of a magnesium AZ31 alloy: examining the role of texture on the deformation mechanisms, Mater. Sci. Eng. A 488 (1) (2008) 406—414.

[7] K. Kondoh, E. Hamada, H. Imai, T. Umeda, J. Jones, Microstructures and mechanical responses of powder metallurgy non-combustive magnesium extruded alloy by rapid solidification process in mass production, Mater. Des. 31 (3) (2010) 1540—1546.

[8] D.C. Foley, M. Al-Maharbi, K.T. Hartwig, I. Karaman, L.J. Kecskes, S.N. Mathaudhu, Grain refinement vs. crystallographic texture: mechanical anisotropy in a magnesium alloy, Scr. Mater. 64 (2) (2011) 193—196.

[9] M. Al-Maharbi, I. Karaman, I.J. Beyerlein, D. Foley, K.T. Hartwig, L.J. Kecskes, S.N. Mathaudhu, Microstructure, crystallographic texture, and plastic anisotropy evolution in an Mg alloy during equal channel angular extrusion processing, Mater. Sci. Eng. A 528 (25) (2011) 7616—7627.

[10] S.R. Agnew, M.H. Yoo, C.N. Tome, Application of texture simulation to understanding mechanical behavior of Mg and solid solution alloys containing Li or Y, Acta Mater. 49 (20) (2001) 4277—4289.

[11] N. Stanford, M.R. Barnett, The origin of "rare earth" texture development in extruded Mg-based alloys and its effect on tensile ductility, Mater. Sci. Eng. A 496 (1) (2008) 399—408.

[12] K. Hantzsche, J. Bohlen, J. Wendt, K.U. Kainer, S.B. Yi, D. Letzig, Effect of rare earth additions on microstructure and texture development of magnesium alloy sheets, Scr. Mater. 63 (7) (2010) 725—730.

[13] S. Agnew, J. Senn, J. Horton, Mg sheet metal forming: lessons learned from deep drawing Li and Y solid-solution alloys, J. Miner. Met. Mater. Soc. 58 (5) (2006) 62—69.

[14] J.R. Rice, The localization of plastic deformation, in: W.T. Koiter (Ed.), Theoretical and Applied Mechanics Proceedings of the 14th International Congress on Theoretical and Applied Mechanics. Delft, The Netherlands. September, 1976, North-Holland Publishing Co., 1977, pp. 207—220.

[15] R. Hill, Acceleration waves in solids, J. Mech. Phys. Solids 10 (1) (1962) 1—16.

[16] Z. Marciniak, K. Kuczyński, Limit strains in the processes of stretch-forming sheet metal, Int. J. Mech. Sci. 9 (9) (1967) 609—620.

[17] R. Sowerby, J.L. Duncan, Failure in sheet metal in biaxial tension, Int. J. Mech. Sci. 13 (3) (1971) 217—229.

[18] Z. Marciniak, K. Kuczyński, T. Pokora, Influence of the plastic properties of a material on the forming limit diagram for sheet metal in tension, Int. J. Mech. Sci. 15 (10) (1973) 789—800.

[19] J.W. Hutchinson, K.W. Neale, Sheet necking-II. Time-independent behavior, in: D.P. Koistinen, N.M. Wang (Eds.), Mechanics of Sheet Metal Forming: Material Behavior and Deformation Analysis: 1977 GMR Symposium, Plenum Press, 1978, pp. 127—153.

[20] R.J. Asaro, A. Needleman, Overview no. 42 Texture development and strain hardening in rate dependent polycrystals, Acta Metall. 33 (6) (1985) 923—953.

[21] H. Yao, J. Cao, Prediction of forming limit curves using an anisotropic yield function with prestrain induced backstress, Int. J. Plast. 18 (8) (2002) 1013—1038.

[22] Karlsson Hibbitt, A.B.A.Q.U.S. Sorensen, Explicit: User's Manual, vol. 1, Hibbitt, Karlsson and Sorenson Incorporated, 2010.

[23] R. Hielscher, H. Schaeben, A novel pole figure inversion method: specification of the MTEX algorithm, J. Appl. Crystallogr. 41 (6) (2008) 1024—1037.

[24] C.A. Bronkhorst, S.R. Kalidindi, L. Anand, Polycrystalline plasticity and the evolution of crystallographic texture in FCC metals, Philos. Trans. R. Soc. Lond. Ser. A Phys. Sci. Eng. 341 (1662) (1992) 443—477.

[25] S. Graff, W. Brocks, D. Steglich, Yielding of magnesium: from single crystal to polycrystalline aggregates, Int. J. Plast. 23 (12) (2007) 1957—1978.

[26] S.R. Kalidindi, Incorporation of deformation twinning in crystal plasticity models, J. Mech. Phys. Solids 46 (2) (1998) 267—290.

[27] A. Staroselsky, L. Anand, A constitutive model for hcp materials deforming by slip and twinning: application to magnesium alloy AZ31B, Int. J. Plast. 19 (10) (2003) 1843—1864.

[28] Y. Chang, D.M. Kochmann, A variational constitutive model for slip-twinning interactions in hcp metals: application to single-and polycrystalline magnesium, Int. J. Plast. 73 (2015) 39—61.

[29] G. Proust, C.N. Tomé, A. Jain, S.R. Agnew, Modeling the effect of twinning and detwinning during strain-path changes of magnesium alloy AZ31, Int. J. Plast. 25 (5) (2009) 861—880.

[30] I.J. Beyerlein, R.J. McCabe, C.N. Tomé, Effect of microstructure on the nucleation of deformation twins in polycrystalline high-purity magnesium: a multi-scale modeling study, J. Mech. Phys. Solids 59 (5) (2011) 988—1003.

[31] N. Bertin, C.N. Tomé, I.J. Beyerlein, M.R. Barnett, L. Capolungo, On the strength of dislocation interactions and their effect on latent hardening in pure magnesium, Int. J. Plast. 62 (2014) 72—92.

[32] C.J. Neil, S.R. Agnew, Crystal plasticity-based forming limit prediction for non-cubic metals: application to Mg alloy AZ31B, Int. J. Plast. 25 (3) (2009) 379—398.

[33] H. Wang, P.D. Wu, K.P. Boyle, K.W. Neale, On crystal plasticity formability analysis for magnesium alloy sheets, Int. J. Solids Struct. 48 (6) (2011) 1000—1010.

[34] D. Steglich, Y. Jeong, Texture-based forming limit prediction for mg sheet alloys ZE10 and AZ31, Int. J. Mech. Sci. 117 (2016) 102—114.

[35] C. Schwindt, F. Schlosser, M.A. Bertinetti, M. Stout, J.W. Signorelli, Experimental and visco-plastic self-consistent evaluation of forming limit diagrams for anisotropic sheet metals: an efficient and robust implementation of the mk model, Int. J. Plast. 73 (2015) 62—99.

[36] R. Becker, J.T. Lloyd, A reduced-order crystal model for HCP metals: application to Mg, Mech. Mater. 98 (2016) 98—110.

[37] J.T. Lloyd, R. Becker, Stress-based crystal analysis of yielding in rolled Mg AZ31B, Philos. Mag. 96 (4) (2016) 370—386.

[38] C.S. Meredith, J.T. Lloyd, T. Sano, The quasi-static and dynamic response of fine-grained Mg alloy AMX602: an experimental and computational study, Mater. Sci. Eng. A 673 (2016) 73—82.

[39] J. Zhang, S.P. Joshi, Phenomenological crystal plasticity modeling and detailed micromechanical investigations of pure magnesium, J. Mech. Phys. Solids 60 (5) (2012) 945—972.

[40] F. Barlat, Crystallographic texture, anisotropic yield surfaces and forming limits of sheet metals, Mater. Sci. Eng. 91 (1987) 55—72.

[41] F. Djavanroodi, M. Janbakhsh, Formability and characterization of titanium alloy sheets, in: J. Sieniawski (Ed.), Titanium Alloys - Advances in Properties Control, InTech, 2013.

[42] M. Kuroda, V. Tvergaard, Forming limit diagrams for anisotropic metal sheets with different yield criteria, Int. J. Solids Struct. 37 (37) (2000) 5037—5059.

[43] M. Kuroda, V. Tvergaard, Effects of texture on shear band formation in plane strain tension/compression and bending, Int. J. Plast. 23 (2) (2007) 244—272.

[44] E. Kelley, W. Hosford, Plane-strain compression of magnesium and magnesium alloy crystals, Trans. Metall. Soc. AIME 242 (1) (1968) 5—13.

[45] Z. Wu, W. Curtin, The origins of high hardening and low ductility in magnesium, Nature 526 (7571) (2015) 62—67.

[46] Z. Wu, W. Curtin, Mechanism and energetics of čaž dislocation cross-slip in hcp metals, Proc. Natl. Acad. Sci. 113 (40) (2016) 201603966.

[47] J. Lévesque, K. Inal, K.W. Neale, R.K. Mishra, Numerical modeling of formability of extruded magnesium alloy tubes, Int. J. Plast. 26 (1) (2010) 65—83.

[48] W. Hosford, A generalized isotropic yield criterion, J. Appl. Mech. 39 (2) (1972) 607—609.

[49] F. Chen, T. Huang, C. Chang, Deep drawing of square cups with magnesium alloy AZ31 sheets, Int. J. Mach. Tools Manuf. 43 (15) (2003) 1553—1559.

[50] F. Abu-Farha, N. Shuaib, M. Khraisheh, K. Weinmann, Limiting strains of sheet metals obtained by pneumatic stretching at elevated temperatures, CIRP Annals Manuf. Technol. 57 (1) (2008) 275—278.

[51] E. Hsu, J. Carsley, R. Verma, Development of forming limit diagrams of aluminum and magnesium sheet alloys at elevated temperatures, J. Mater. Eng. Perform. 17 (3) (2008) 288—296.

[52] H. Kim, S. Choi, K. Lee, H. Kim, Experimental determination of forming limit diagram and springback characteristics of AZ31B Mg alloy sheets at elevated temperatures, Mater. Trans. 49 (5) (2008) 1112—1119.

[53] J. Min, L. Hector, J. Lin, J. Carter, Analytical method for forming limit diagram prediction with application to a magnesium ZEK100-O alloy, J. Mater. Eng. Perform. 22 (11) (2013) 3324—3336.

[54] S. Kurukuri, M. Worswick, A. Bardelcik, R. Mishra, J. Carter, Constitutive behavior of commercial grade ZEK100 magnesium alloy sheet over a wide range of strain rates, Metall. Mater. Trans. A 45 (8) (2014) 3321—3337.